ELSEVIER

Contents lists available at ScienceDirect

Sensors and Actuators: B. Chemical

journal homepage: www.elsevier.com/locate/snb





Silver nanotriangle array based LSPR sensor for rapid coronavirus detection

Yanjun Yang a,*, Jackelyn Murray b, James Haverstick c, Ralph A. Tripp b, Yiping Zhao c

- a School of Electrical and Computer Engineering, College of Engineering, The University of Georgia, Athens, GA 30602, USA
- ^b Department of Infectious Diseases, College of Veterinary Medicine, University of Georgia, Athens, GA 30602, USA
- ^c Department of Physics and Astronomy, The University of Georgia, Athens, GA 30602, USA

ARTICLE INFO

Keywords: Silver nanotriangle array Localized surface plasmon resonance (LSPR) Coronavirus detection SARS-CoV-2 spike receptor binding domain Coronavirus NL63

ABSTRACT

A rapid, portable, and cost-effective method to detect the infection of SARS-CoV-2 is fundamental toward mitigating the current *COVID-19* pandemic. Herein, a human angiotensin-converting enzyme 2 protein (ACE2) functionalized silver nanotriangle (AgNT) array localized surface plasmon resonance (LSPR) sensor is developed for rapid coronavirus detection, which is validated by SARS-CoV-2 spike RBD protein and CoV NL63 virus with high sensitivity and specificity. A linear shift of the LSPR wavelength versus the logarithm of the concentration of the spike RBD protein and CoV NL63 is observed. The limits of detection for the spike RBD protein, CoV NL63 in buffer and untreated saliva are determined to be 0.83 pM, 391 PFU/mL, and 625 PFU/mL, respectively, while the detection time is found to be less than 20 min. Thus, the AgNT array optical sensor could serve as a potential rapid point-of-care COVID-19 diagnostic platform.

1. Introduction

The SARS-CoV-2 pandemic COVID-19 disease has led to unprecedented burden on national and international healthcare. This has motivated researchers to develop reliable tools to aid SARS-CoV-2 diagnostics. The current molecular diagnostic tests for SARS-CoV-2 can be classified into two categories, i.e., nucleic acid tests and serological/ immunological tests. The identification of SARS-CoV-2 typically involves viral RNA based reverse transcriptase real-time polymerase chain reaction (RT-PCR) and nucleic acid hybridization strategies [1,2]. RT-PCR is the 'gold standard' and has excellent selectivity and sensitivity and is laboratory-based [3], but this detection requires viral RNA extraction and expertise in PCR which is time-consuming and requires qualified personnel. Similarly, immunological tests may take days-to-weeks after the onset of symptoms for a patient to develop a detectable antibody level [4]. Although the IgM/IgG rapid test kits are available, false-positive results may occur[5]. Recently, direct detection of SARS-CoV-2 using reverse transcription loop-mediated isothermal amplification (RT-LAMP) on heat-inactivated samples has become available [6]. However, the development of rapid and highly accurate biosensors for coronavirus (CoV) is still needed. Table S1 in the Supplementary Materials (SM) summarizes some of the recent development and the corresponding sensing performance. Among different proposed methods, localized surface plasmon resonance (LSPR)-based optical

sensors are one of the potential entrants as a rapid SARS-CoV-2 sensor, have attracted notable attention and been widely studied over the past decade [7–9]. The resonance absorbance wavelength of the LSPR sensor responds to changes in the local dielectric environment. These sensors are compact, durable, repeatable, and more reliable than traditional sensors, offering real-time and label-free chemical and biological detection. Label-free LSPR biosensors for SARS-CoV-2 screening have been reported for nucleic acids [10,11], surface protein subunits (spike, envelope, and membrane) [12], and SARS-CoV-2 virus[13,14], as well as antibodies (IgG, IgM) [15-17]. For example, Ventura et al. proposed a colorimetric sensor using gold nanoparticles for SARS-CoV-2 surface spike protein detection [12]. Huang et al. developed a double-antibody sandwich plasmonic resonance immunoassay for SARS-CoV-2 pseudovirus detection using Au nanocup array chip and gold nanoparticles, and reported a LOD of 370 virus particle/mL [14]. But this sandwich detection strategy and sensor preparations are complicated. Very recently, an aptamer-functionalized gold nanoparticle based sensor was reported and was able to detect 16 nM spike protein and 3.54×10^6 genome copies/mL of inactivated SARS-CoV-2[13]. However, sliver should have a higher plasmonic effect compared to Au [18]. And the rapid and cost-effective LSPR sensor chips still need to be developed for direct detections of SARS-CoV-2 or coronavirus (CoV).

In this study, a human angiotensin-converting enzyme 2 protein (ACE2) functionalized silver nanotriangle (AgNT) array LSPR sensor is

E-mail address: YanjunYang@uga.edu (Y. Yang).

 $^{^{\}ast}$ Corresponding author.

developed with high sensitivity and specificity of SARS-CoV-2 spike RBD proteins and CoV NL63. A linear shift of the LSPR wavelength versus the logarithm of spike RBD protein concentration is observed in the concentration region from 2.03 pM to 9420 pM. For NL63, the detection range extended from 625 to 10^4 PFU/mL in untreated saliva. The detection time is determined to be less than 20 min. This rapid optical sensor can be expanded as a potential point-of-care COVID-19 diagnostic platform for real sample analysis.

2. Materials and methods

2.1. Materials

Polystyrene nanospheres (PSNS) with 500 nm diameter (Polyscience, Lot# 679675) were used to form the colloid monolayer onto clean glass slides (Gold Seal, Part# 301). Sulfuric acid (Fisher Scientific, 98%), ammonium hydroxide (Fisher Scientific, 98%), and hydrogen peroxide (Fisher Scientific, 30%) were acquired to clean the glass slides. Silver (Kurt J. Lesker, 99.999%) and titanium pellets (Kurt J. Lesker, 99.995%) were purchased as the evaporation materials. Methanol, acetone, 1-hexanol (Tokyo Chemical Industry Co., >98%), chloroform (J.T. Baker, 99%), tetrachloromethane (Sigma-Aldrich, 99.9%), and toluene (Fisher Scientific, 99.8%) were used to characterize the refractive index (RI) sensing performance of the AgNT array. Human angiotensin-converting enzyme 2 protein (Sino Biological) and SARS-CoV-2 spike receptor binding domain protein (spike RBD; Sino Biological) were purchased for surface functionalization and sensing application. Bovine serum albumin (Sigma) was purchased for surface blocking. Sodium phosphate dibasic (Na₂HPO₄; ≥99.0%), sodium phosphate monobasic (NaH₂PO₄; ≥99.0%), sodium chloride (NaCl; ≥99.0%), trehalose, mannitol, and Tween-80 were purchased from Sigma. PBS buffer (100 mM Na₂HPO₄,

 $100~\text{mM}~\text{NaH}_2\text{PO}_4,\,300~\text{mM}~\text{NaCl},\,pH=7.4),$ phosphate buffer ($100~\text{mM}~\text{Na}_2\text{HPO}_4$ and $100~\text{mM}~\text{NaH}_2\text{PO}_4,\,pH=7.4)$ and dilution buffer (1 mL PBS containing 0.05 g trehalose, 0.05 g mannitol, 0.1 µL Tween-80) were prepared and used for the treatment of proteins. Dulbecco's Modified Eagles Medium (DMEM; GIBCO BRL laboratories, Grand Island, NY) supplemented with 1% fetal bovine serum (FBS; Hyclone Laboratories, Salt Lake City, UT) was used as cell culture media. Deionized (DI) water (18 M Ω cm) was used throughout all the experiments. All chemicals and materials were used without further purification.

2.2. Sensing strategy

The general sensing strategy is shown in Fig. 1. It consists of four steps: Step 1: AgNT array fabrication. Step 2: ACE2 immobilization. Step 3: BSA blocking. Step 4: spike RBD protein or virus detection.

2.3. Fabrication of AgNT array

The general fabrication procedure is outlined in Fig. S1A. Prior to PSNS monolayer formation, the glass substrates (2.54 cm \times 0.9 cm) were cleaned with sulfuric acid, ammonium hydroxide, and hydrogen peroxide. All substrates were then rinsed in deionized water. The uniform PSNS (diameter 500 nm) monolayers with large monocrystalline domains were prepared on glass substrates via an air-water interface method[19]. The PSNS monolayer-coated substrates were loaded into a custom-designed electron beam deposition system with the substrate normal antiparallel to the incident vapor direction. The vacuum chamber was pumped down under a base pressure of $<10^{-6}$ Torr. A 3 nm layer of Ti was deposited at a rate of 0.2 nm/s followed by a 60 nm Ag film deposited at 0.3 nm/s under a high vacuum condition. The

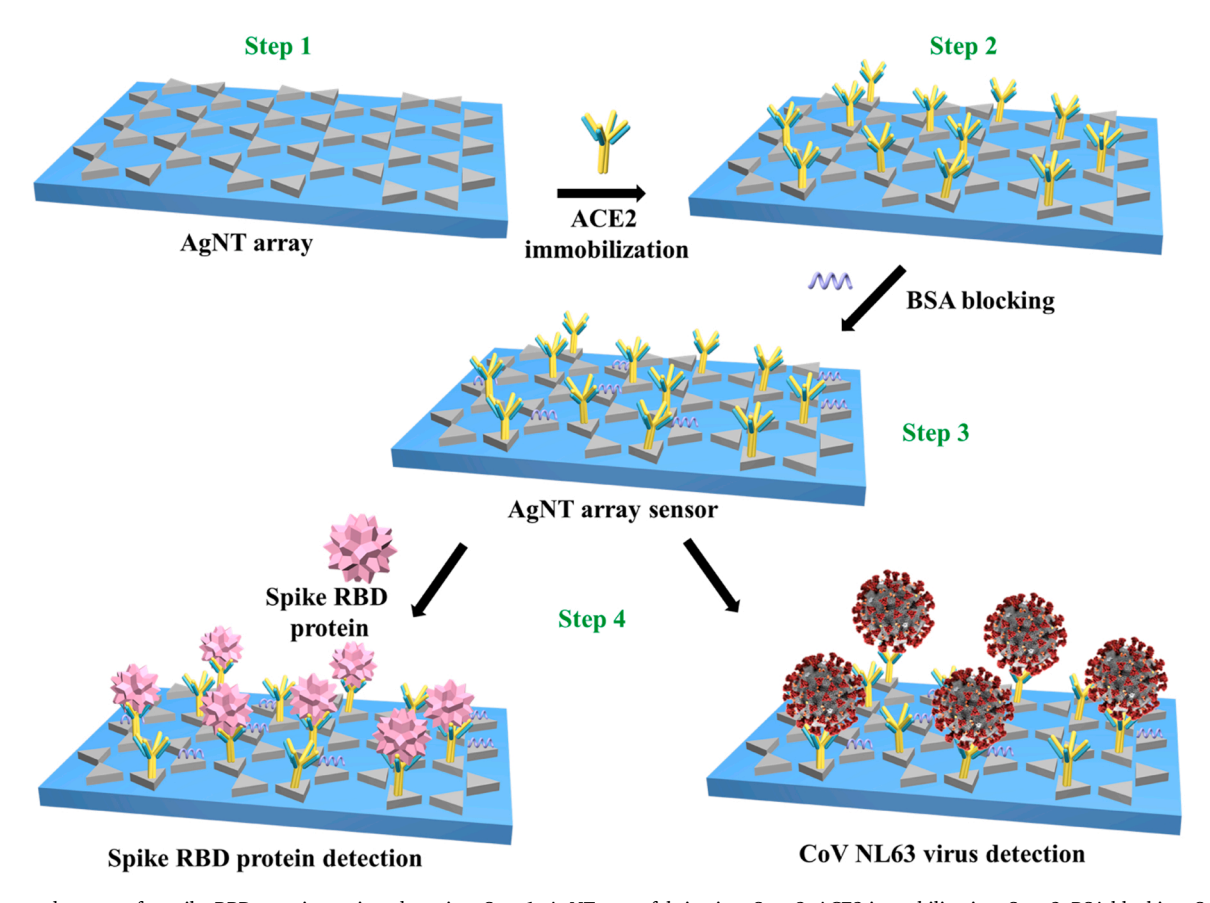


Fig. 1. Proposed strategy for spike RBD protein or virus detection. Step 1: AgNT array fabrication. Step 2: ACE2 immobilization. Step 3: BSA blocking. Step 4: spike RBD protein or CoV detection.

deposition rate and vapor thickness on the substrate were monitored by a quartz crystal microbalance. After the Ag deposition, the monolayer template was removed using Scotch tape, and the substrates were rinsed in toluene, acetone, and 2-propanol to remove PSNS residue. Subsequently, a PDMS layer with arrayed small wells (3 wells, with the well diameter of 4 mm, well depth of 1 mm) was molded on the AgNT array to restrict the effective sensing areas (Fig. S1B), and we refer them as AgNT wells.

2.4. Immobilization of ACE2 on AgNT array

The ACE2 protein was immobilized on the AgNT array via electrostatic and hydrophobic interactions. First, 200 μL ACE2 protein at 0.62 mg/mL was dialyzed in phosphate buffer (100 mM Na2HPO4 and 100 mM NaH2PO4, pH = 7.4). The dialyzed ACE2 solution was diluted to 66 $\mu g/mL$ with phosphate buffer. 20 μL ACE2 solution was transferred into each AgNT well and incubated for 2 h at room temperature. Then, the wells were washed with DI water 3 times. Subsequently, 20 μL of 1 mg/mL BSA solution was transferred to a AgNT well and incubated for 2 h in order to block the ACE2 uncovered area of AgNT and avoid nonspecific binding of spike RBD protein or virus particles. Subsequently, the wells were rinsed with DI water and air-dried. The ACE2 protein modified AgNT array substrates (AgNT sensors) were now ready for the detection. The corresponding optical transmission spectra of the same AgNT well was measured after each step of surface modification.

2.5. Spike RBD protein detection

 $20~\mu L$ spike RBD protein ranging from 2.03 pM to 9420 pM in dilution buffer were transferred into different ACE2 functionalized AgNT wells and incubated for 2 h at room temperature. Then, the AgNT array sensors were washed with DI water and air-dried for optical transmission measurements.

2.6. Virus incubation

All the virus experiments, including virus preparation, characterization, and LSPR measurements, were conducted in a biosafety level 2 (BSL-2) environment. CoV NL63, CoV 229E, and CoV OC43 were propagated in Vero E6 cells which were maintained in DMEM supplemented with 1% heat-inactivated (56 °C) FBS. Briefly, cells were infected using a multiplicity of infection (MOI) = 0.1. After 48 h, the viruses were harvested in serum-free DMEM followed by two freezethaws (-70 °C/4 °C), after which the contents were collected and centrifuged at 4000 g for 15 min at 4 $^{\circ}$ C. The virus titers were similar, i. e., 10⁵ PFU/mL, determined by immunostaining plaque assay as previously described [20]. Table S2 lists the different kinds of coronavirus as well as corresponding receptors. There are three kinds of coronavirus, CoV NL63, SARS-CoV, SARS-CoV-2, which are specific to ACE2 protein. The experiments on SARS-CoV and SARS-CoV-2 must be conducted in BSL-3 lab, while CoV OC43, CoV 229E, and CoV NL63 can be handled in BSL-2 environment.

2.7. Coronavirus (CoV) detection

CoV NL63, CoV 229E or CoV OC43 cell-free supernatant suspensions ranging from 391 to 10^5 PFU/mL in PBS buffer were transferred into different ACE2 functionalized AgNT wells and incubated for 2 h at room temperature. Subsequently the AgNT wells were washed 3x with DI water and air-dried for optical transmission measurements. Virus spiked saliva samples were prepared by adding different concentrations of CoV NL63 to saliva to achieve final concentrations ranging from 625 to 10^4 PFU/mL for detection. To mimic the non-pretreated saliva sample, saliva samples for each AgNT well were prepared by adding 2 μ L of different concentrations of coronavirus solutions to $18~\mu$ L of saliva, so the original coronavirus solutions were diluted 10~ folds, i.e., the

maximum viral concentration in the saliva sample for detection was only 1×10^4 PFU/mL.

2.8. Instruments

The morphology of the AgNT array was characterized by atomic force microscopy (AFM, Park Systems NX-10 AFM). The optical transmission spectra of the as deposited AgNT arrays were measured by an ultraviolet-visible spectrophotometer (UV-Vis, Jasco-750). For virus detection in a BSL-2 environment, a portable UV-Vis spectrophotometer was used for transmission measurement of CoV detection in a biosafety level-2 hood and a pair of pinholes were added between the incident light and sample surface to restrict the incident light to a smaller area. The setup also consisted of a halogen source (Tungsten Halogen HL-2000), a spectrophotometer (Ocean Optics USB2000) and two optical fibers. The transmission spectra $T_s(\lambda)$ and $T_r(\lambda)$ of AgNT wells and reference sample (bare glass slide) were measured separately, and the final transmission spectra $T(\lambda)$ was calculated as $T(\lambda) = T_s(\lambda)/T_r(\lambda)$.

3. Results and discussion

3.1. Characterization of AgNT array

Fig. S2A shows a representative AFM image of AgNT array fabricated via the 500 nm PSNS monolayer. As expected, equilateral nanotriangle arrays with the side length of 152 \pm 3 nm are formed, and the height of each triangle is 60 ± 1 nm. A distinct dip λ_0 in UV-Vis transmission spectrum (Fig. S2B) is found at $\lambda_0 = 641 \pm 2$ nm, taking from 8 different AgNT samples (Fig. S3). The refractive index (RI) sensitivity of the AgNT array is evaluated by measuring the λ_0 shift when the AgNT array is immersed in solutions with different refractive indices, and the corresponding transmission spectra are shown in Fig. S2C. The change of λ_0 versus refractive index (RI) is plotted in Fig. S2D, and the slope gives the sensitivity of the LSPR sensor, $S=210\pm10$ nm/RIU, where RIU refers to refractive index unit. A similar sensitivity of 191 nm/RIU has been reported for a similar structure[21]. Even though this AgNT array does not have a high RI sensitivity, the AgNT array is straightforward to fabricate and has large uniform area. The nanofabrication procedure for AgNT array is relatively inexpensive compared to gold nanostructures or other nanostructures fabricated either by focus ion beam method or by electron beam lithography method.

3.2. Optimize ACE2 protein immobilization on the AgNT array

ACE2 is the cellular receptor for NL63, SARS-CoV, and SARS-CoV-2 [22]. Previous studies have demonstrated that the S1 domains of coronaviruses contain the receptor-binding domains (RBDs) that directly bind to the cellular receptors [23]. To achieve specific detection of spike RBD protein and NL63, ACE2 protein is used to functionalize the AgNT array. However, Ag is not chemically stable in NaCl solution [24], rather is found to be stable in phosphate buffer (see Section S1 in SM). Thus, phosphate buffer was used to dialyze the ACE2 solution to remove the chloride ions and for further ACE2 immobilization. To optimize the ACE2 protein immobilization on the AgNT array, 20 µL ACE2 solutions of a series of concentrations ranging from 4.96 to 124 $\mu g/mL$ were transferred into different AgNT wells. Transmission spectra of AgNT wells were measured before and after the ACE2 immobilization. The redshift of λ_0 , i.e., $\Delta \lambda = \lambda_{ACE2} - \lambda_0$, versus different concentration C_{ACE2} of ACE2 protein is plotted in Fig. 2A. The $\Delta\lambda$ initially increases rapidly with C_{ACE2} when C_{ACE2} is small; then approaches to a constant when $C_{ACE2} > 40$ µg/mL. This relationship follows the Langmuir isotherm adsorption model for proteins [25],

$$\Delta \lambda = \Delta \lambda_{max} \left(\frac{kC_{ACE2}}{1 + kC_{ACE2}} \right), \tag{1}$$

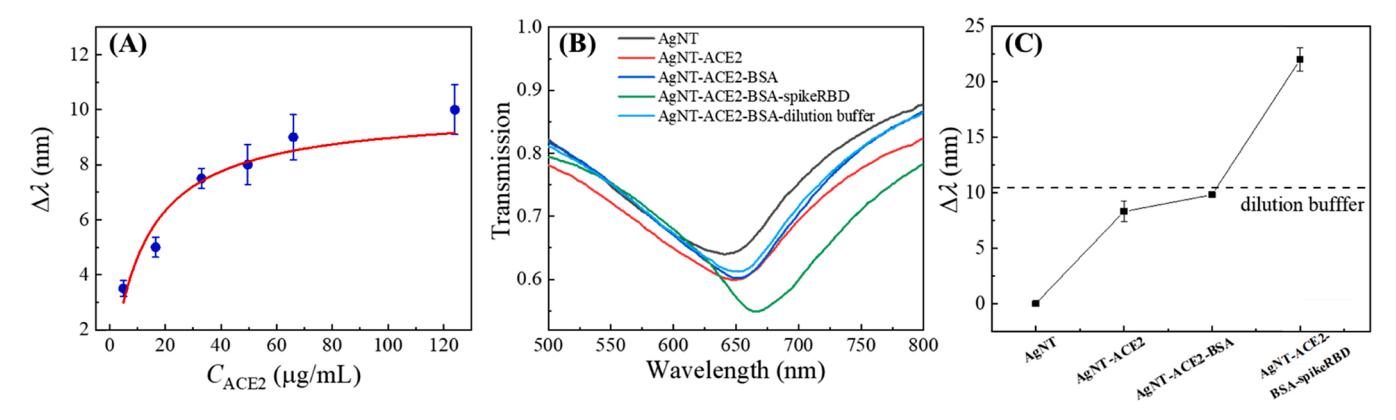


Fig. 2. (A) The plot of the shift of LSPR wavelength $\Delta\lambda$ of AgNT array versus the different concentration C_{ACE2} of ACE2 protein. (B) The transmission spectra of AgNT array at different stages of surface functionalization and detection: immobilized with ACE2 protein, BSA blocking, spike RBD protein detection at $C_{spikeRBD} = 675$ pM as well as AgNT array sensor incubating with dilution buffer. (C) Corresponding LSPR wavelength change $\Delta\lambda$.

where $\Delta \lambda_{max}$ is the maximum LSPR shift measured when the ACE2 protein is fully covering the AgNT and k is the surface binding constant of the ACE2 to Ag surface. The solid curve in Fig. 2A shows the best fitting with $k = 0.08 \pm 0.03 \text{mL/µg}$ and $\Delta \lambda_{max} = 10 \pm 1 \text{nm}$. The adsorption of ACE2 protein on the silver surface is mainly dependent on electrostatic interaction and the Ag-S covalent bond [26]. ACE2 proteins can bind to silver surfaces through either free amine groups or cysteine residues in the proteins and via the electrostatic attraction of negatively charged carboxylate groups. Those amino acids with residues containing sulfur atoms can form covalent bonds with silver. The binding constant is influenced by these factors as well as the surface coverage of the Ag film. According to the fitting, for $C_{ACE2} > 66 \,\mu\text{g/mL}$, the $\Delta\lambda$ (= 8.3nmat $C_{ACE2} = 66 \, \mu \text{g/mL}$) does not change too much. Therefore, C_{ACE2} = 66 μg/mL of ACE2 has been selected as the optimized immobilization concentration. The success of the ACE2 immobilization on Ag surface was further confirmed by the surface enhance Raman scattering (SERS) spectroscopy as shown in Section S2 of SM.

The spike RBD detection is performed following the four steps shown in Fig. 1, and the corresponding transmission spectra and $\Delta\lambda$ change for each step are shown in Fig. 2B. When AgNT array is incubated with 66 µg/mL ACE2 protein, the $\Delta\lambda$ red shifts 8.3 \pm 0.9 nm (measured from 20 AgNT wells, see Fig. S5), indicating that ACE2 proteins have been immobilized on the AgNT array. The assembly of ACE2 protein results in a change of the dielectric constant of microenvironment. After BSA blocking, λ_0 further red shifts 1.5 nm. Such a small change in $\Delta \lambda$ indicates that the BSA only blocks a small fraction of the AgNT surface area. When adding spike RBD protein of a concentration $C_{spikeRBD}$ = 675 pM, λ_0 further increases 12.0 \pm 0.4 nm, indicating that the spike RBD proteins bind to ACE2 proteins. Compared $\Delta \lambda$ between adding spike RBD protein and BSA blocking, this AgNT array sensor shows good specificity for spike RBD protein detection. Here, prior to the spike RBD detection, the buffer for spike RBD protein incubation has been optimized as shown in Fig. S6. The dilution buffer (1 mL PBS contains 0.05 g trehalose, 0.05 g mannitol, 0.1 µL tween-80) gave the maximum LSPR shift and was used in all reported results for spike RBD protein incubation. When only adding dilution buffer without spike RBD protein, λ_0 only red shifts around 1 nm (the dashed line in Fig. 2 C), which is within the accuracy of the detection system. Also, with only the PBS buffer, the LSPR wavelength $\Delta\lambda$ does not blue shift, which demonstrates that ACE2 and BSA protein can protect the silver surface from degradation in the biological environment. So, the functionalized AgNT array sensor is reliable for biosensing applications.

3.3. Spike RBD protein detection

The above result shows that the AgNT LSPR sensor can specifically detect spike RBD protein. Further $C_{spikeRBD}$ dependence experiments

have been conducted and the $\Delta\lambda$ versus $C_{spikeRBD}$ plot is shown in Fig. 3A along with the original UV-Vis spectra. In a semi-log plot, the $\Delta\lambda$ seems to increase linearly with $\log_{10}C_{spikeRBD}$ (Fig. 3B). A good linear relationship is found in the $C_{spikeRBD}$ region from 2.03 pM to 9420 pM, and the best fitting gives $\Delta\lambda_{spikeRBD}=3.7\times \log[C_{spikeRBD}]+1.8$ (nm), where the goodness of fitting R^2 is 0.978. Defining the limit of detection (LOD) as the lowest detected concentration whose signal is higher than the blank control signal plus three standard deviations [27,28], the LOD of spike RBD protein is estimated to be 0.83 pM. This is comparable with those obtained by other methods, including commercial ELISA kits, that usually fall in the pM concentration range [29]. In addition, the total detectable range spans in 4 orders of magnitude, from \sim 1 pM to 10^4 pM, and the actual amount of spike RBD molecules in the detection light beam area is estimated to be from 3×10^4 to 2×10^9 molecules shown in Table S4.

The stability of the AgNT array sensor has also been examined. ACE2 immobilized AgNT array sensors were stored in sealed opaque pouches filled with argon gas and kept at 20 °C for three weeks, then the optical transmission spectra of the ACE2 modified AgNT samples (Fig. S8A) as well as treated by spike RBD protein ($C_{spikeRBD}=2020\,$ pM, Fig. S8B) were measured. As shown in Fig. S8A, there is almost no change in λ_0 in AgNT samples after stored for one and three weeks, compared to that of the freshly prepared AgNT samples. Similar result is found for the samples incubating with spike RBD protein solutions (Fig. S8B), and the corresponding redshifts $\Delta\lambda$ were found to be $14.0\pm0.5\,$ nm, $12.5\,$

 \pm 0.6 nm, and 14.5 \pm 0.3 nm, respectively (Fig. S8C), which are comparable to the result reported in Fig. 3B.

3.4. Specificity of AgNT array sensor for CoVs

To test the specificity of AgNT array sensor, similar detection experiments have been performed on the three strains of CoV, i.e., 229E, OC43, and NL63 at the same concentration of 10^5 PFU/mL in DMEM with 1% FBS. Fig. 4A shows the corresponding transmission spectra and the $\Delta\lambda$ is plotted in Fig. 4B. The $\Delta\lambda$ caused by DMEM buffer (with 1% FBS) is around 1 nm, and the average $\Delta\lambda$ for 229E and OC43 is around 2 nm, which is significantly lower compared to $\Delta\lambda=40$ nm for NL63. Such a difference demonstrates that the ACE2 is highly specified to CoV NL63.

3.5. Specific detection of NL63 in PBS and in untreated saliva

Fig. 4 C shows that the LSPR wavelength λ_0 redshifts continuously after being incubated with NL63 of different concentrations, ranging from 391 to 10^5 PFU/mL in PBS buffer. PBS solution with no NL63 was used as the blank. The semi-log concentration dependent $\Delta\lambda_{\rm NL63}$ plot in

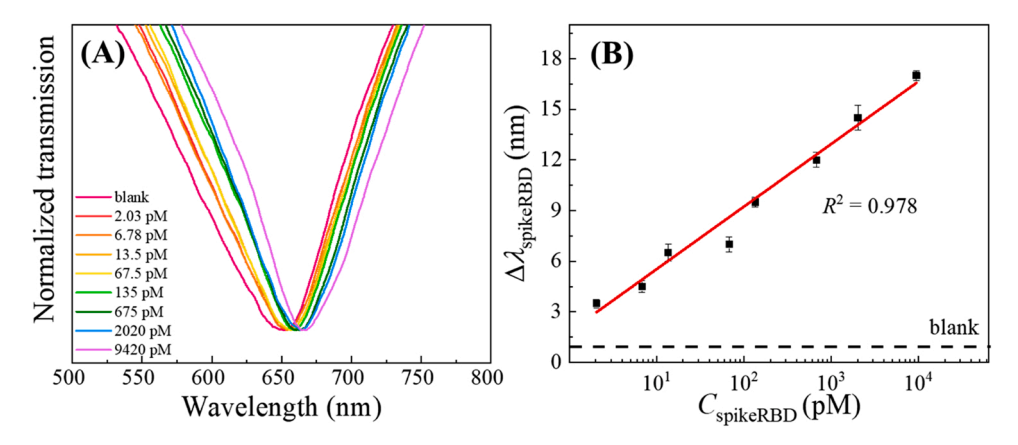


Fig. 3. (A) The normalized concentration-dependent transmission spectra for $C_{\rm spikeRBD}=2.03$ pM to 9420 pM. (B) A semi-log plot of the LSPR wavelength shift $\Delta\lambda_{\rm spikeRBD}$ versus $C_{\rm spikeRBD}$. The solid line is the fitting result.

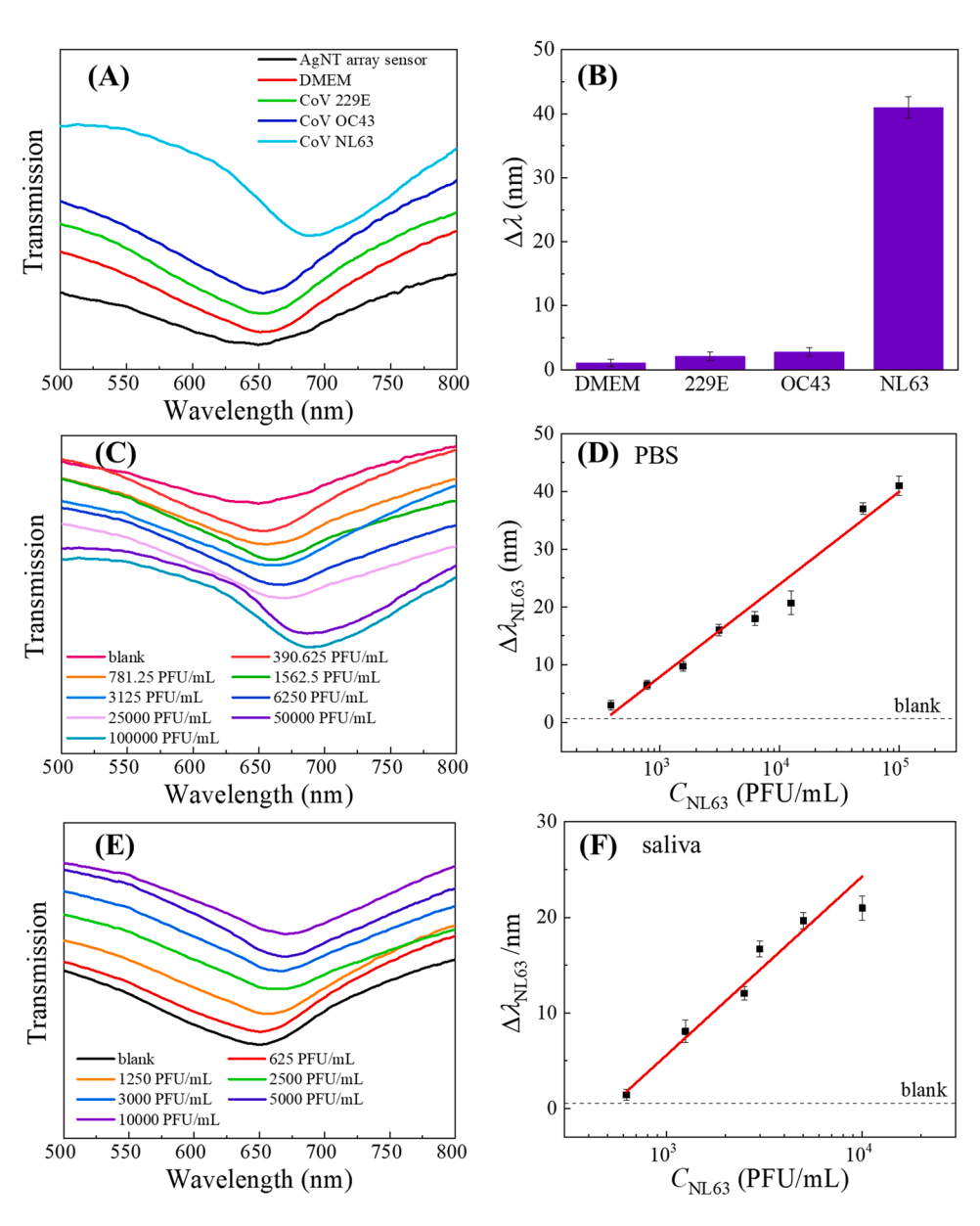


Fig. 4. (A) The transmission spectra of the AgNT wells treated with DMEM buffer (with 1% FBS), 229E, OC43, and NL63 at the concentration of 10^5 PFU/mL, and (B) the corresponding $\Delta\lambda$ plot. (C) The concentration-dependent transmission spectra of NL63 detection ranging from 391 to 10^5 PFU/mL in PBS buffer, and (D) the semi-log plot of $\Delta\lambda_{\rm NL63}$ versus $C_{\rm NL63}$. (E) The concentration-dependent transmission spectra of NL63 detection ranging from 625 to 10^4 PFU/mL in untreated saliva, and (F) the corresponding semi-log plot of $\Delta\lambda_{\rm NL63}$ versus $C_{\rm NL63}$.

Fig. 4D also demonstrates a linear relationship, which can be written as $\Delta \lambda_{NL63}(nm) = m \log[C_{NL63}] + \Delta \lambda_0$, where m characterizes the apparent sensitivity of the AgNT sensor and $\Delta \lambda_0$ is the initial LSPR wavelength shift. For NL63 detection in PBS buffer, $m^{PBS} =$ 16 ± 1 nm/log($\frac{PFU}{mI}$), $\Delta \lambda_0 = -40 \pm 4$ nm with $R^2 = 0.981$, and the LOD is 391 PFU/mL. The good reproducibility of AgNT array sensor has been demonstrated as shown in Section S3 of SM. Considering the serious matrix effects of high concentration saliva, NL63 was added in 90% saliva to prepare NL63 spiked saliva samples with different concentrations. Saliva without adding NL63 was used as the blank. The good detection ability of the AgNT array sensor is again demonstrated in untreated saliva. As shown in Fig. 4F, a linear relationship in the semilog plot is found ranging from 625 to 10^4 PFU/mL with m^{saliva} = 19 ± 2 nm/log $[f_0](\frac{PFU}{mL})$, $\Delta \lambda_0 = -51 \pm 6$ nm with $R^2 = 0.965$. The LOD is 625 PFU/mL. These results show that the apparent sensitivities of the AgNT sensor, m^{PBS} and m^{saliva} , for NL63 detection in different environments, are very similar, which indicates that the AgNT array sensor has good performance in complex biological environments. For the LOD, as shown in Table S1 for different sensors, the LODs are given in different units and there is no definite relationship between different units. For example, PFU/mL, copies of RNA, or number of viral particles/mL. In general, one tends to assume that one PFU corresponds to one viral particle and one viral particle only contains one RNA [30,31]. However, there are exceptions, for example, the PFU/viral particle ratio for varicella-zoster virus is 40,000:1 [32] and the RNA copies to viral particle varies for different variants of CoV-SARS-2 viruses[33]. In order to have a systematic comparison, a side-by-side PCR measurements and LSPR measurements should be conducted in order to obtain a more qualitative relationship.

3.6. Estimation of the number of detected viruses on AgNT

Based on the detection strategy shown in Fig. 1, the whole detection process can be considered as coating the AgNT with two dielectric layers as shown in Fig. 5A. The first coated layer is a uniform layer of ACE2 protein with an RI $n_p=1.45[34,35]$. BSA blocking can be ignored or included in the first layer, because the $\Delta\lambda$ of BSA blocking is only 1.5 nm. The second layer is NL63 with refractive index of each particle $n_v=1.8[36]$. According to Li et al., the electric field in the surrounding layers decays exponentially from the surface of AgNT with a characteristic decay length $\delta[37]$. Therefore, the effective refractive index of each coated layer is integrated by the local refractive index from zero to infinity [21,38],

$$n_{e\!f\!f} = rac{2}{\delta} \int_0^\infty n(x) e^{-rac{2x}{\delta}} dx, \quad ext{with} n(x) = \left\{egin{array}{l} n_p, 0 < x \leq d_p \\ n_t, d_p < x \leq d_p + d_t \\ n_a, x > d_p + d_t \end{array}
ight\},$$
 (2).

where n_p is RI of ACE2 layer, n_t is RI of NL63 viral particle layer, n_a is RI of air, d_p is the thickness of ACE2 layer, and d_t is the thickness of NL63 layer. Based on the ACE2 immobilization,

$$\Delta \lambda_{ACE2} = S(n_p - n_a)(1 - e^{-\frac{2dp}{\delta}}),\tag{3}$$

where $\Delta \lambda_{ACE2} = 10 \pm 1$ nm, $S = 210 \pm 10$ nm/RIU, $n_p = 1.45$, $n_a = 1$, $d_p = 5$ nm[22], then δ can be estimated to be 89.4 nm, which is similar to the value reported in Ag nanohole array [39]. When the sensor captures the virus, $\Delta \lambda$ can be written as,

$$\Delta \lambda = S(n_t - n_a)e^{-\frac{2dp}{\delta}} (1 - e^{-\frac{2d_t}{\delta}}) \tag{4}$$

Therefore, the effective RI of the virus layer can be estimated as,

$$n_t = \frac{\Delta \lambda_{lspr}}{Se^{\frac{-2d_p}{\delta}} (1 - e^{-\frac{2d_t}{\delta}})} + n_a.$$
 (5)

Here we take $d_t=100$ nm, since the transmission electron microscopic (TEM) studies of NL63 infected LLCMK2 cells revealed that virions were spherical, spiked, and range from 75 to 115 nm in diameter [40]. Based on Fig. 4D, the effective n_t versus C_{NL63} is estimated, as plotted in Fig. S12A. The viral layer is a porous layer, not totally covered by the virus particles. Its RI can be estimated by the effective medium theory, the Bruggeman's equation [41],

$$\delta_{\nu} \left(\frac{\varepsilon_{\nu} - \varepsilon_{t}}{\varepsilon_{\nu} + \varepsilon_{t}} \right) + \left(1 - \delta_{\nu} \right) \left(\frac{\varepsilon_{a} - \varepsilon_{t}}{\varepsilon_{a} + \varepsilon_{t}} \right) = 0, \tag{6}$$

where ε_t , ε_ν and ε_a are the effective dielectric constants of the medium, the dielectric constant of the NL63 virus, and the dielectric constant of air, respectively, and δ_ν is the volume fraction of the NL63. Also, $\varepsilon_t = n_t^2$, δ_ν can be written as

$$\delta_{\nu} = \frac{\binom{n_{\alpha}^{2} - n_{r}^{2}}{n_{\alpha}^{2} + n_{r}^{2}}}{\binom{n_{\alpha}^{2} - n_{r}^{2}}{n_{\alpha}^{2} + n_{r}^{2}}} - \binom{n_{\gamma}^{2} - n_{r}^{2}}{n_{\nu}^{2} + n_{r}^{2}}}.$$
(7)

The experimentally obtained δ_v versus C_{NL63} is plotted in Fig. S12B. If the NL63 viral particle is assumed to be a sphere, then the number of viral particles that are detectable on each individual AgNT can be estimated based on Fig. 4D. As shown in Fig. 5B, at the LOD, every AgNT has an average of one viral particle bonded. At the highest detectable concentration (10⁵ PFU/mL), each AgNT has an average 12 virus particles bonded. According to the area of an AgNT, the total number of virus particles available on an AgNT is estimated to be around 32. So, there is still room for the sensor to detect higher virus concentrations.

3.7. The time-dependent detection of spike RBD and NL63 $\,$

The detection time of AgNT array sensor is mainly determined by the ACE2-SpikeRBD or ACE2-virus binding time. To assess the real detection time for the AgNT LSPR sensor, systematic investigations have been performed. First, the AgNT array sensor was incubated with 20 μ L spikeRBD at $C_{spikeRBD} = 2020$ pM for varied time duration t. The purple

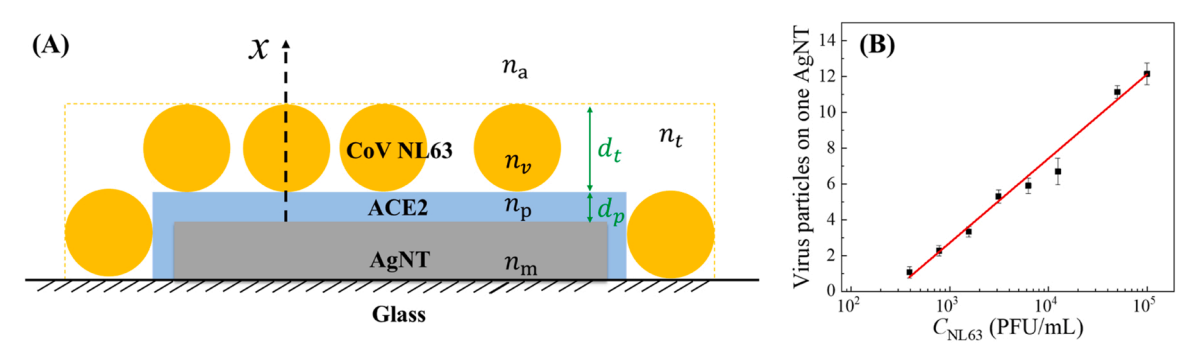


Fig. 5. (A) The scheme of coronavirus detection model. (B) The semi-log plot and linear fitting of the virus particles on one AgNT versus C_{NL63}.

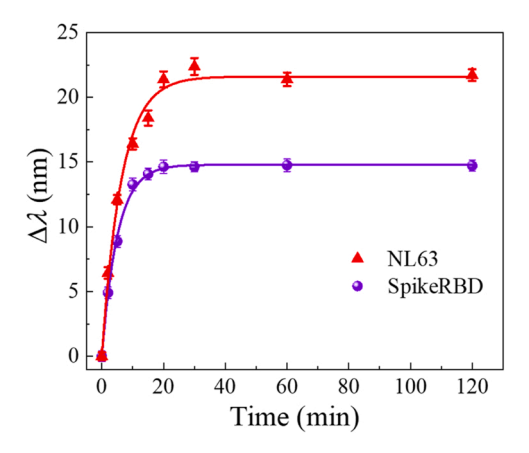


Fig. 6. The time-dependent detection of spike RBD (circles) at $C_{spikeRBD} = 2020$ pM and NL63 (triangles) at $C_{NL63} = 12,500$ PFU/mL. The solid curves are fitting results based on Eq. (8).

circles in the Fig. 6 plot $\Delta\lambda_{\rm spikeRBD}$ as a function of t. When t < 20 min, $\Delta\lambda_{\rm spikeRBD}$ red shifts almost monotonically with t, while when $t \geq 20$ min, the $\Delta\lambda_{\rm spikeRBD}$ reaches a saturation value, $\Delta\lambda_{\rm spikeRBD}^S = 14.7 \pm 0.5$ nm. At t = 5 min, a distinct $\Delta\lambda_{\rm spikeRBD}$ (= 8.9 ± 0.5 nm) can be observed, while at t = 10 min, $\Delta\lambda_{\rm spikeRBD}$ (= 13.3 ± 0.5 nm) is near 90% of the saturation $\Delta\lambda_{\rm spikeRBD}^S$. Such a trend is consistent with molecular binding kinetics on a surface, which can be written as

$$\Delta \lambda = \Delta \lambda^s (1 - e^{-\frac{t}{\rho}}),\tag{8}$$

where $\Delta\lambda^s$ is the saturation wavelength shift and t^0 is the binding time constant. For spike RBD protein detection at $C_{spikeRBD}=2020$ pM, $\Delta\lambda_{spikeRBD}^S$ can be obtained as 14.8 ± 0.2 nm, and $t_{spikeRBD}^0$ is 5.1 ± 0.2 min. Similarly, the AgNT array sensor was incubated with 20 µL NL63 at $C_{\text{NL63}}=12,500$ PFU/mL for various t. The red triangles in the Fig. 6 plot $\Delta\lambda_{\text{NL63}}$ as a function of t, and a trend similar to that of $\Delta\lambda_{\text{spikeRBD}}$ -t is observed. Based on Eq. (8), $\Delta\lambda_{NL63}^S=21.6\pm0.4$ nm and $t_{NL63}^0=6.4\pm0.4$ min are obtained. The $t_{spikeRBD}^0$ is slightly smaller than t_{NL63}^0 , indicating that spike RBD protein of SARS-CoV-2 binds faster to ACE2. Both results indicate that the AgNT based sensor has a detection time of less than 20 min

4. Conclusions

In summary, an ACE2 functionalized AgNT array LSPR sensor has been developed and shown to have a high specificity to SARS-CoV-2 and NL63. The LSPR sensor can detect the SARS-CoV-2 spike RBD protein and NL63 virus with high sensitivity and selectivity. For all these detections, the shift of the LSPR wavelength follows a linear relationship with the logarithm of the concentration of spike RBD proteins and NL63. For the spike RBD protein, the detection is observed in the concentration region from 2.03-9420 pM. For the NL63, lowest detection concentration (LOD) is found to be 391 PFU/mL in PBS buffer. This sensor can also detect NL63 in untreated saliva with a slightly higher LOD of 625 PFU/ mL. The detection time is governed by the ACE2-viron particle binding time, and systematical experiments have shown it to be $< 20 \ \text{min}$ for both spike RBD protein and NL63 detections. This LSPR sensor configuration is very simple and many of the measurements can be performed using a handheld UV-Vis spectrometer (Ocean Optics USB2000). In principle, any LSPR sensor can adopt the proposed strategy in Fig. 1 for spike RBD protein or coronavirus detection.

In fact, most works reported in the literature (see Table S1) are concentrated on spike protein detection, and only few really report the results on real virus detection [42–44]. Among them, only four works

focused on plasmonic based sensors [12–14,45]. Though the LOD of our sensor on spike RBD detection is significantly higher than the graphene-based field-effect transistor sensor [42] and cell-based sensor [46] (but lower than that of the electrochemical immunoassay [47]), the fabrication and detection instrument for our sensors are much more simplified and cost effective. For the virus sensing, the LOD of our sensor is comparable to or better that of the plasmonic sensor [14] and the electrochemical immunoassay [48]. In addition, the viral particles used in Refs. [14,49] are SARS-CoV-2 pseudotyped viral particles or inactivated virus, not the real virus. Our estimation on the number of viral particle binding shows that at the LOD, every AgNT has an average of one viral particle bonded, which further confirms the reliability of our detection.

Clearly this AgNT sensor has the following advantages: first, the fabrication procedure for AgNT array is straightforward and inexpensive; second, the AgNT array can be fabricated into a large and uniform area; and finally, the sensor measurement can be fulfilled by a handheld UV-Vis spectrometer. In addition, AgNT should have a higher plasmonic effect compared to Au. However, the structure of the AgNT is not optimized for sensitivity. By varying the composition and size of the AgNT, one could significantly improve the sensitivity of the LSPR sensor from $\sim 210 \ \text{nm/RIU}$ to $\sim 700 \ \text{nm/RIU}$ or possibly better[50,51], thus lowering the LOD. With improvements, a fast and cost-effective optical sensor can be expected as a potential point-of-care SARS-CoV-2 diagnostic platform for sample analysis.

CRediT authorship contribution statement

Yanjun Yang: Conceptualization, Methodology, Investigation, Writing. Jackelyn Murray: Methodology, Investigation. James Haverstick: Methodology, Investigation. Ralph A. Tripp: Conceptualization, Methodology, Writing, Funding acquisition, Supervision. Yiping Zhao: Conceptualization, Methodology, Writing, Funding acquisition, Supervision.

Declaration of Competing Interest

The authors declare that they have no known competing financial interests or personal relationships that could have appeared to influence the work reported in this paper.

Acknowledgements

Yanjun Yang, James Haverstick, and Yiping Zhao were partially supported by a National Science Foundation grant under the Grant No. ECCS-1808271. Ralph A. Tripp and Jackelyn Murray were supported by the Georgia Research Alliance.

Supplementary materials

Supplementary data to this article can be found online at: A diagram of the AgNT array fabrication procedure; the basic characterization of the LSPR AgNT sensor; the transmission spectra of multiple AgNT wells; the exploration of the optimized buffer for spike RBD protein detection; the stability test of the AgNT array sensor; the calculation of the number of spike RBD molecules in the light beam during the detection via AgNT well; modeling for virus detection; estimation of the full coverage of virus on a single AgNT.

Appendix A. Supporting information

Supplementary data associated with this article can be found in the online version at doi:10.1016/j.snb.2022.131604.

References

- [1] B. Udugama, P. Kadhiresan, H.N. Kozlowski, A. Malekjahani, M. Osborne, V.Y. C. Li, et al., Diagnosing COVID-19: The disease and dools for detection, ACS Nano 14 (2020) 3822–3835.
- [2] T. Nolan, R.E. Hands, S.A. Bustin, Quantification of mRNA using real-time RT-PCR, Nat. Protoc. 1 (2006) 1559–1582.
- [3] M. Alafeef, K. Dighe, P. Moitra, D. Pan, Rapid, ultrasensitive, and quantitative detection of SARS-CoV-2 using antisense oligonucleotides directed electrochemical biosensor chip, ACS Nano 14 (2020) 17028–17045.
- [4] N. Ravi, D.L. Cortade, E. Ng, S.X. Wang, Diagnostics for SARS-CoV-2 detection: a comprehensive review of the FDA-EUA COVID-19 testing landscape, Biosens. Bioelectron. 165 (2020), 112454.
- [5] Z. Li, Y. Yi, X. Luo, N. Xiong, Y. Liu, S. Li, et al., Development and clinical application of a rapid IgM-IgG combined antibody test for SARS-CoV-2 infection diagnosis, J. Med. Virol. 92 (2020) 1518–1524.
- [6] A. Alekseenko, D. Barrett, Y. Pareja-Sanchez, R.J. Howard, E. Strandback, H. Ampah-Korsah, et al., Direct detection of SARS-CoV-2 using non-commercial RT-LAMP reagents on heat-inactivated samples, Sci. Rep. 11 (2021) 1820.
- [7] M.E. Stewart, C.R. Anderton, L.B. Thompson, J. Maria, S.K. Gray, J.A. Rogers, et al., Nanostructured plasmonic sensors, Chem. Rev. 108 (2008) 494–521.
- [8] K.M. Mayer, J.H. Hafner, Localized surface plasmon resonance sensors, Chem. Rev. 111 (2011) 3828–3857.
- [9] M. Li, S.K. Cushing, N. Wu, Plasmon-enhanced optical sensors: a review, Analyst 140 (2015) 386–406.
- [10] P. Moitra, M. Alafeef, K. Dighe, M.B. Frieman, D. Pan, Selective naked-eye detection of SARS-CoV-2 mediated by N gene targeted antisense oligonucleotide capped plasmonic nanoparticles, ACS Nano 14 (2020) 7617–7627.
- [11] G. Qiu, Z. Gai, Y. Tao, J. Schmitt, G.A. Kullak-Ublick, J. Wang, Dual-functional plasmonic photothermal biosensors for highly accurate severe acute respiratory syndrome coronavirus 2 detection, ACS Nano 14 (2020) 5268–5277.
- [12] B.D. Ventura, M. Cennamo, A. Minopoli, R. Campanile, S.B. Censi, D. Terracciano, et al., Colorimetric test for fast detection of SARS-CoV-2 in nasal and throat swabs, ACS Sens. 5 (2020) 3043–3048.
- [13] S. Aithal, S. Mishriki, R. Gupta, R.P. Sahu, G. Botos, S. Tanvir, et al., SARS-CoV-2 detection with aptamer-functionalized gold nanoparticles, Talanta 236 (2022), 122841.
- [14] L. Huang, L. Ding, J. Zhou, S. Chen, F. Chen, C. Zhao, et al., One-step rapid quantification of SARS-CoV-2 virus particles via low-cost nanoplasmonic sensors in generic microplate reader and point-of-care device, Biosens. Bioelectron. 171 (2021). 112685.
- [15] T.T.S. Lew, K.M.M. Aung, S.Y. Ow, S.N. Amrun, L. Sutarlie, L.F.P. Ng, et al., Epitope-functionalized gold nanoparticles for rapid and selective detection of SARS-CoV-2 IgG antibodies, ACS Nano 15 (2021) 12286–12297.
- [16] R. Funari, K.-Y. Chu, A.Q. Shen, Detection of antibodies against SARS-CoV-2 spike protein by gold nanospikes in an opto-microfluidic chip, Biosens. Bioelectron. 169 (2020). 112578.
- [17] A.N. Masterson, B.B. Muhoberac, A. Gopinadhan, D.J. Wilde, F.T. Deiss, C.C. John, et al., Multiplexed and high-throughput label-free detection of RNA/spike protein/ IgG/IgM biomarkers of SARS-CoV-2 infection utilizing nanoplasmonic biosensors, Anal. Chem. 93 (2021) 8754–8763.
- [18] K. Khurana, N. Jaggi, Localized surface plasmonic properties of Au and Ag nanoparticles for sensors: a review, Plasmonics 16 (2021) 981–999.
- [19] W.M. Ingram, C. Han, Q. Zhang, Y. Zhao, Optimization of Ag-coated polystyrene nanosphere substrates for quantitative surface-enhanced Raman spectroscopy analysis, J. Phys. Chem. C. 119 (2015) 27639–27648.
- [20] A. Tripp Ralph, D. Moore, L. Jones, W. Sullender, J. Winter, J. Anderson Larry, Respiratory syncytial virus G and/or SH protein alters Th1 cytokines, natural killer cells, and neutrophils responding to pulmonary infection in BALB/c mice, J. Virol. 73 (1999) 7099–7107.
- [21] A.J. Haes, R.P. Van Duyne, A nanoscale optical biosensor: sensitivity and selectivity of an approach based on the localized surface plasmon resonance spectroscopy of triangular silver nanoparticles, J. Am. Chem. Soc. 124 (2002) 10596–10604.
- [22] R. Yan, Y. Zhang, Y. Li, L. Xia, Y. Guo, Q. Zhou, Structural basis for the recognition of SARS-CoV-2 by full-length human ACE2, Science 367 (2020) 1444.
- [23] J. Babcock Gregory, J. Esshaki Diana, D. Thomas William, D.M. Ambrosino, Amino acids 270 to 510 of the severe acute respiratory syndrome coronavirus spike protein are required for interaction with receptor, J. Virol. 78 (2004) 4552–4560.
- [24] J.X. Fu, A. Collins, Y.P. Zhao, Optical properties and biosensor application of ultrathin silver films prepared by oblique angle deposition, J. Phys. Chem. C. 112 (2008) 16784–16791.
- [25] J.C. Riboh, A.J. Haes, A.D. McFarland, C. Ranjit Yonzon, R.P. Van Duyne, A nanoscale optical biosensor: real-time immunoassay in physiological buffer enabled by improved nanoparticle adhesion, J. Phys. Chem. B 107 (2003) 1772-1780
- [26] A. Gole, C. Dash, V. Ramakrishnan, S.R. Sainkar, A.B. Mandale, M. Rao, et al., Pepsin-gold colloid conjugates: preparation, characterization, and enzymatic activity, Langmuir 17 (2001) 1674–1679.
- [27] Z. Wang, S. Zong, W. Li, C. Wang, S. Xu, H. Chen, et al., SERS-fluorescence joint spectral encoding using organic-metal-QD hybrid nanoparticles with a huge encoding capacity for high-throughput biodetection: putting theory into practice, J. Am. Chem. Soc. 134 (2012) 2993–3000.
- [28] G.F. Wang, R.J. Lipert, M. Jain, S. Kaur, S. Chakraboty, M.P. Torres, et al., Detection of the potential pancreatic cancer marker MUC4 in serum using surfaceenhanced Raman scattering, Anal. Chem. 83 (2011) 2554–2561.

- [29] S. Zhang, A. Garcia-D'Angeli, J.P. Brennan, Q. Huo, Predicting detection limits of enzyme-linked immunosorbent assay (ELISA) and bioanalytical techniques in general, Analyst 139 (2014) 439–445.
- [30] A. Yakimovich, V. Andriasyan, R. Witte, I.H. Wang, V. Prasad, M. Suomalainen, et al., Plaque2.0 a high-throughput analysis framework to score virus-cell transmission and clonal cell expansion, PLoS One 10 (2015), e0138760.
- [31] S.J. Martin, The biochemistry of viruses: CUP Archive; 1978.
- [32] E. Carpenter John, P. Henderson Ernesto, C. Grose, Enumeration of an extremely high particle-to-PFU ratio for varicella-zoster virus, J. Virol. 83 (2009) 6917–6921.
- [33] H.W. Despres, M.G. Mills, D.J. Shirley, M.M. Schmidt, M.-L. Huang, K.R. Jerome, et al., Quantitative measurement of infectious virus in SARS-CoV-2 Alpha, Delta and Epsilon variants reveals higher infectivity (viral titer:RNA ratio) in clinical samples containing the Delta and Epsilon variants, medRxiv, (2021) 2021.09.07.21263229.
- [34] E. Özkumur, J.W. Needham, D.A. Bergstein, R. Gonzalez, M. Cabodi, J. M. Gershoni, et al., Label-free and dynamic detection of biomolecular interactions for high-throughput microarray applications, Proc. Natl. Acad. Sci. U.S.A. 105 (2008) 7988.
- [35] J. Piehler, A. Brecht, G. Gauglitz, Affinity detection of low molecular weight analytes, Anal. Chem. 68 (1996) 139–143.
- [36] A.M. Hamed, Image processing of corona virus using interferometry, Opt. Photonics J. 6 (2016) 75.
- [37] Y. Li, Plasmonic Optics: Theory and Applications, SPIE, Washington, USA, 2017.
- [38] L.S. Jung, C.T. Campbell, T.M. Chinowsky, M.N. Mar, S.S. Yee, Quantitative interpretation of the response of surface plasmon resonance sensors to adsorbed films, Langmuir 14 (1998) 5636–5648.
- [39] B. Ai, P. Basnet, S. Larson, W. Ingram, Y. Zhao, Plasmonic sensor with high figure of merit based on differential polarization spectra of elliptical nanohole array, Nanoscale 9 (2017) 14710–14721.
- [40] J.M. Orenstein, B. Banach, S.C. Baker, Morphogenesis of coronavirus HCoV-NL63 in cell culture: A transmission electron microscopic study, Open Infect. Dis. J. 2 (2008) 52–58.
- [41] R. Landauer, Electrical conductivity in inhomogeneous media, AIP Conf. Proc. 40 (1978) 2–45.
- [42] G. Seo, G. Lee, M.J. Kim, S.-H. Baek, M. Choi, K.B. Ku, et al., Rapid Detection of COVID-19 causative virus (SARS-CoV-2) in human nasopharyngeal swab specimens using field-effect transistor-based biosensor, ACS Nano 14 (2020) 5135–5142.
- [43] S. Kim, H. Ryu, S. Tai, M. Pedowitz, J.R. Rzasa, D.J. Pennachio, et al., Real-time ultra-sensitive detection of SARS-CoV-2 by quasi-freestanding epitaxial graphenebased biosensor, Biosens. Bioelectron. 197 (2022), 113803.
- [44] D.K. Agarwal, V. Nandwana, S.E. Henrich, V.P.V.N. Josyula, C.S. Thaxton, C. Qi, et al., Highly sensitive and ultra-rapid antigen-based detection of SARS-CoV-2 using nanomechanical sensor platform, Biosens. Bioelectron. 195 (2022), 113647.
- [45] N. Cennamo, L. Pasquardini, F. Arcadio, L. Lunelli, L. Vanzetti, V. Carafa, et al., SARS-CoV-2 spike protein detection through a plasmonic D-shaped plastic optical fiber aptasensor, Talanta 233 (2021), 122532.
- [46] S. Mavrikou, G. Moschopoulou, V. Tsekouras, S. Kintzios, Development of a Portable, Ultra-rapid and ultra-sensitive cell-based biosensor for the direct detection of the SARS-CoV-2 S1 spike protein antigen, Sensors 20 (2020) 3121.
- [47] L. Fabiani, M. Saroglia, G. Galatà, R. De Santis, S. Fillo, V. Luca, et al., Magnetic beads combined with carbon black-based screen-printed electrodes for COVID-19: A reliable and miniaturized electrochemical immunosensor for SARS-CoV-2 detection in saliva, Biosens. Bioelectron. 171 (2021), 112686.
- [48] H. Yousefi, A. Mahmud, D. Chang, J. Das, S. Gomis, J.B. Chen, et al., Detection of SARS-CoV-2 viral particles using direct, reagent-free electrochemical sensing, J. Am. Chem. Soc. 143 (2021) 1722–1727.
- [49] J. Li, A. Wuethrich, S. Edwardraja, R.J. Lobb, S. Puttick, S. Rose, et al., Amplification-free SARS-CoV-2 detection using nanoyeast-scFv and ultrasensitive plasmonic nanobox-integrated nanomixing microassay, Anal. Chem. 93 (2021) 10251–10260.
- $\begin{tabular}{ll} \textbf{[50]} & S. Larson, Y. Zhao, Localized surface plasmonic resonance and sensing properties of $$Ag-MgF_2$ composite nanotriangles, J. Phys. Chem. C. 122 (2018) 7374–7381. \end{tabular}$
- [51] S. Larson, Z. Yang, Y. Zhao, Improving LSPR sensing performance using multilayered composition graded Ag-Cu nanotriangle arrays, Chem. Commun. 55 (2019) 1342–1344.

Yanjun Yang is a PhD student in the College of Engineering at the University of Georgia under the supervision of Prof. Yiping Zhao. Her current research focuses on the fabrication, characterization, and application of plasmonic nanomaterials for SERS/LSPR based sensors for chemical and biological analysis.

Jackelyn Murray is a Research Professional in the Department of Infectious Diseases at the University of Georgia. Her Research interests include understanding the mechanisms of immunity and disease pathogenesis associated with respiratory virus infection.

James Haverstick is an undergraduate student in the Department of Physics and Astronomy at the University of Georgia under the supervision of Prof. Yiping Zhao. His current research focuses on the development of plasmonic nanomaterials for SERS/LSPR based biosensing.

Ralph A. Tripp joined the University of Georgia in 2004 from the Centers of Disease Control and Prevention (CDC) in Atlanta. He is a Professor and Georgia Research Alliance Eminent Scholar working in vaccine and therapeutic studies in the Department of

Infectious Diseases at UGA. Research interests include understanding the mechanisms of immunity and disease pathogenesis associated with respiratory virus infection and using this information to develop therapeutic protocols and vaccines that will confer long-term protective immunity.

Yiping Zhao is a Distinguished Research Professor at the Department of Physics and Astronomy and an adjunct professor at the College of Engineering in University of Georgia. He is a fellow of SPIE and AVS. His research interests are nanostructures and thin films fabrication and characterization, plasmonic nanostructures, chemical and biological sensors, nano-photocatalysts, and nanomotors.